



**HAL**  
open science

## Crack initiation and propagation in braided SiC/SiC composite tubes: effect of braiding angle

Yang Chen, Lionel Gélebart, Camille Chateau, Michel Bornert, Andrew King, Cédric Sauder, Patrick Aïmedieu

### ► To cite this version:

Yang Chen, Lionel Gélebart, Camille Chateau, Michel Bornert, Andrew King, et al.. Crack initiation and propagation in braided SiC/SiC composite tubes: effect of braiding angle. *Journal of the European Ceramic Society*, 2020, 40 (13), pp.4403-4418. 10.1016/j.jeurceramsoc.2020.04.060 . hal-02870690

**HAL Id: hal-02870690**

**<https://enpc.hal.science/hal-02870690v1>**

Submitted on 16 Jun 2020

**HAL** is a multi-disciplinary open access archive for the deposit and dissemination of scientific research documents, whether they are published or not. The documents may come from teaching and research institutions in France or abroad, or from public or private research centers.

L'archive ouverte pluridisciplinaire **HAL**, est destinée au dépôt et à la diffusion de documents scientifiques de niveau recherche, publiés ou non, émanant des établissements d'enseignement et de recherche français ou étrangers, des laboratoires publics ou privés.

## Crack initiation and propagation in braided SiC/SiC composite tubes: effect of braiding angle

Yang Chen<sup>1,2</sup>, Lionel Gélébart<sup>1</sup>, Camille Chateau<sup>2</sup>, Michel Bornert<sup>2</sup>, Andrew King<sup>3</sup>, Cédric Sauder<sup>1</sup>, Patrick Aïmedieu<sup>2</sup>

<sup>1</sup>DEN-Service de Recherches Métallurgiques Appliquées, CEA, Université Paris-Saclay, F-91191, Gif-sur-Yvette, France

<sup>2</sup>Laboratoire Navier, UMR 8205, Ecole des Ponts ParisTech, IFSTTAR, CNRS, Université Paris-Est, F-77455 Marne-la-Vallée, France

<sup>3</sup>Synchrotron SOLEIL, St-Aubin 91192, France

### Abstract

Crack initiation and propagation in three braided SiC/SiC composite tubes with different braiding angles are investigated by in situ tensile tests with synchrotron micro-computed tomography. Crack networks are precisely detected after an image subtraction procedure based on Digital Volume Correlation. FFT based simulations are performed on the full-resolution 3D images to assess elastic stress/strain fields. Quantitative measurements of the crack geometries are performed using a novel method based on grey levels. The results show that braiding angle has no obvious effect on the location of crack onsets (initiation always occurs at tow interfaces), whereas it significantly affects the paths of crack propagation. This work provides an explicit demonstration of the crack propagation scenarios with respect to the mesoscopic fibre architectures.

### Keywords

Ceramic matrix composites; In situ X-ray computed tomography; FFT simulation; Crack detection; Crack propagation scenario

**NOTICE:** This is the post-peer-review, pre-copyedit version of an article published in Journal of the European Ceramic Society (2020). The final authenticated version is available online at <https://doi.org/10.1016/j.jeurceramsoc.2020.04.060>

## 1. Introduction

According to the concept of new generation nuclear reactors, as well as the accident-tolerant fuels, the temperature around the fuel clads can reach more than 1000°C [1,2]. By virtue of their outstanding high-temperature performance, SiC/SiC composites have been studied since decades as a material alternative to metals in such applications [1–4]. However, due to the microstructural complexity in 3D, the relationship between their macroscopic behaviour and multiscale microstructures is still not fully understood, and this issue remains one of the major obstacles for final applications of SiC/SiC composites in nuclear reactors. Pseudo-

ductile behaviour can be achieved by using appropriate interphase between fibres and matrix [3,5]. Textile fibre architectures are commonly used to produce macroscopic reinforcement in more than one directions. Textile fibre architectures can strongly affect the mechanical behaviour of the composites [6–8], and the most commonly used ones for tubular structural components are filament winding, 2D braiding and triaxial braiding. The mechanical nonlinearity of a SiC/SiC composite is due to the development of micro-cracks inside the microstructure under load. Therefore, it is essential to understand this micro-macro relationship, in order to ensure the material strength to fulfil the in-service conditions in nuclear applications.

Experimental characterisations of the damage mechanisms (micro-cracking) for SiC/SiC composites have been reported in the literature. Elementary damage mechanisms, such as matrix cracking, fibre breaks and fibre-matrix interfacial degradation are usually studied with single-fibre composites [9,10] and unidirectional minicomposites [11,12]. Damage evolution in textile SiC/SiC composites has also been investigated using different experimental approaches, see e.g. [13–21] among others. Some indirect methods, such as electrical resistance [19] and acoustic emission (AE) [13], have been proven convenient to continuously monitor the global damage evolution in the SiC/SiC composites during mechanical loading. However, even though clustering techniques have been proposed (e.g. [14]), precisely distinguishing the damage natures (matrix crack, fibre break, or interfacial degradation) is still difficult. In addition, the damage growth paths in the material microstructure seem very difficult, if not impossible, to be observed using indirect methods. Surface observations at mesoscale with Digital Image Correlation (DIC) was used in [16,17] to analyse the damage evolution in a precise and quantitative way. Yet, the cracks in the composite bulk could not be observed. Others used X-ray micro-computed tomography ( $\mu$ CT) combined with in situ testing and Digital Volume Correlation (DVC), see e.g. [18,20,21]. This is an attractive characterisation approach for studying damage behaviour of composite materials (see [22] for a review), because it provides very rich and direct information on both the 3D microstructure and the micro-cracks with their geometries and spatial distributions. Some recent effort has been put on combining  $\mu$ CT and AE to characterise the evolution of different damage modes, i.e. matrix cracks and fibre breaks [23]. Yet, the generalisation of the observation from the afore-mentioned reference is still not straightforward due to the difficulty in reliably clustering AE signals when dealing with more complex microstructures loaded off the fibre axis.

In this study, in situ tensile tests have been conducted on braided SiC/SiC composite tubes using synchrotron  $\mu$ CT setup. The purpose is to provide relevant experimental arguments for better understanding the damage-microstructure relationship. One particular question is addressed: as an important parameter of braiding process, how does the braiding angle affect the damage initiation and propagation in the SiC/SiC composite tubes? Focus is put on mesoscopic analyses. However, the satisfactory image resolution ( $2.60\sim 2.85\ \mu\text{m}/\text{voxel}$ ) also allows us to discuss the damage mechanisms at smaller length scale, namely fibre break and effect of micropores.

Tubes with three different braiding angles ( $30^\circ$ ,  $45^\circ$  and  $60^\circ$ ) are tested under axial tension and the microstructural changes are recorded in synchrotron tomography images. DVC technique is used to measure the local displacement field. Three-dimensional crack networks are detected after an image subtraction based on the DVC measurements [24]. In order to alleviate the limitations on temporal and spatial resolutions of in situ tomography experiments for the observation of damage initiation, local elastic stress fields are simulated

with full image resolution for the whole field of view, see [25] for details. These large-scale simulations, involving over billions of voxels, are conducted under a HPC (high-performance computing) framework. These simulations employ a massively parallel in-house software AMITEX [26], based on Fast Fourier Transforms. For each tube, the crack propagation scenario is observed in relation with the braided architecture. A novel method [27] is used to quantify two geometric parameters, opening and surface area, of the detected crack networks. Statistical representability of the observations relies on the use of a large field of view containing two or three braid periods in the axial direction and four in the whole circumference of each tube.

## 2. Materials and methods

### 2.1 Materials

The braided SiC/SiC composite tubes have been manufactured at LTMEx/CEA Saclay (France), using three different braiding angles: 30°, 45°, 60° (Figure 1). Each tube has been manufactured from a fibrous preform of two braided layers. Each tow contains about 500 Hi-Nicalon type S fibres. Pyrocarbon interphase and SiC matrix have been sequentially deposited onto the fibrous preforms using Chemical Vapour Infiltration (CVI) process, resulting in similar porosity volume fractions of 17~20% in the three tubes. The inner diameters of the tubes have been controlled to be the same (3.47 mm), while their outer diameters varied with the braiding angle (4.79 mm, 4.89 mm and 5.25 mm for 30°, 45° and 60° tubes, respectively). The outer diameters have been measured by laser micrometre taking the average of maximum (peaks of tows) and minimum (valleys of tows) measured values. The significant difference in outer diameter indicates that the out-of-plane undulation of tows increases with the braiding angle. Residual pores after CVI can be classified into two groups: micropores that are located inside tows having line-like forms and oriented similarly to adjacent fibres, and macropores that are located among tows having tortuous geometries.

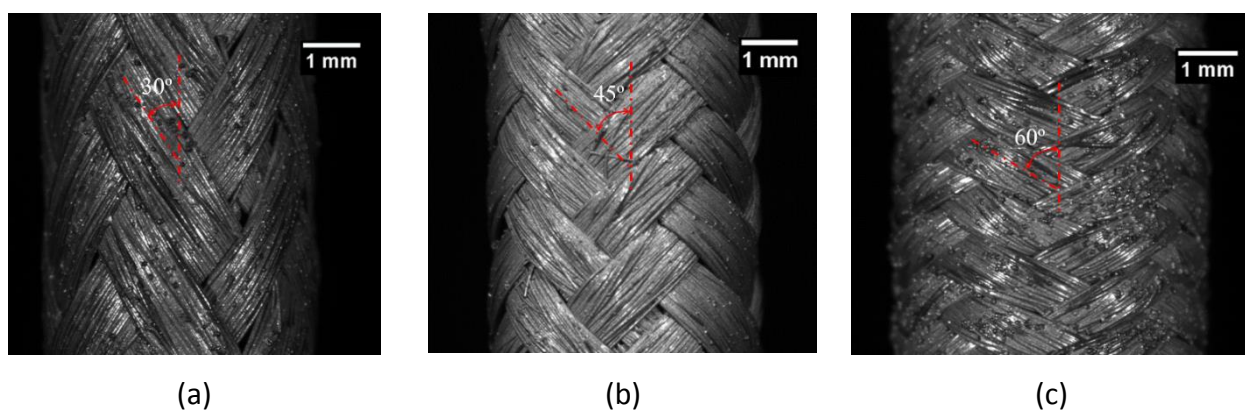


Figure 1. Optical images of the tube surfaces with different braiding angles: (a) 30°, (b) 45°, (c) 60°.

The macroscopic stress-strain curves of the tubes under tension are given in Figure 2, showing a clear braiding angle effect: a larger braiding angle leads to a lower elastic limit, a lower stress to failure but a larger strain to failure. Let us note that the porosity fractions in the different tubes were similar, therefore, this difference in elastic limit should be related to the fibre architecture, as will be discussed in section 3.3. Each type of tubes with the same braiding

angle have been tested twice and their macroscopic responses are very reproducible, except the strains to failure of the 60° tubes (1.3% and 1.6%). These reference curves have helped to choose the stress levels for the incremental in-situ tensile tests.

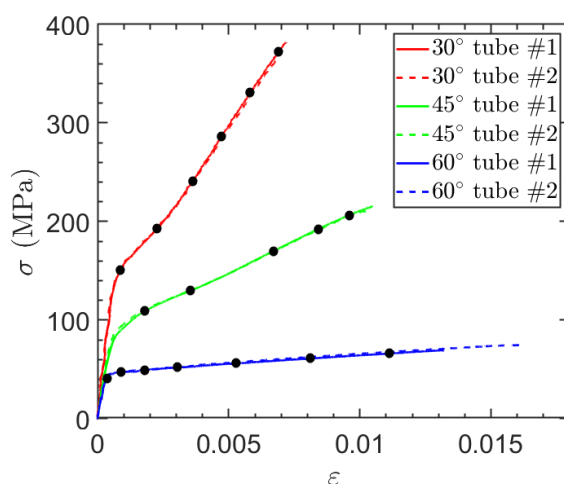


Figure 2. The macroscopic stress-strain curves under tension for the tubes with three different braiding angles: 30°, 45°, 60°. Two tubes of each braiding angle have been tested to check the reproducibility of the macroscopic behaviour. The black dots mark the loading steps at which the tubes have been scanned during the in situ tests.

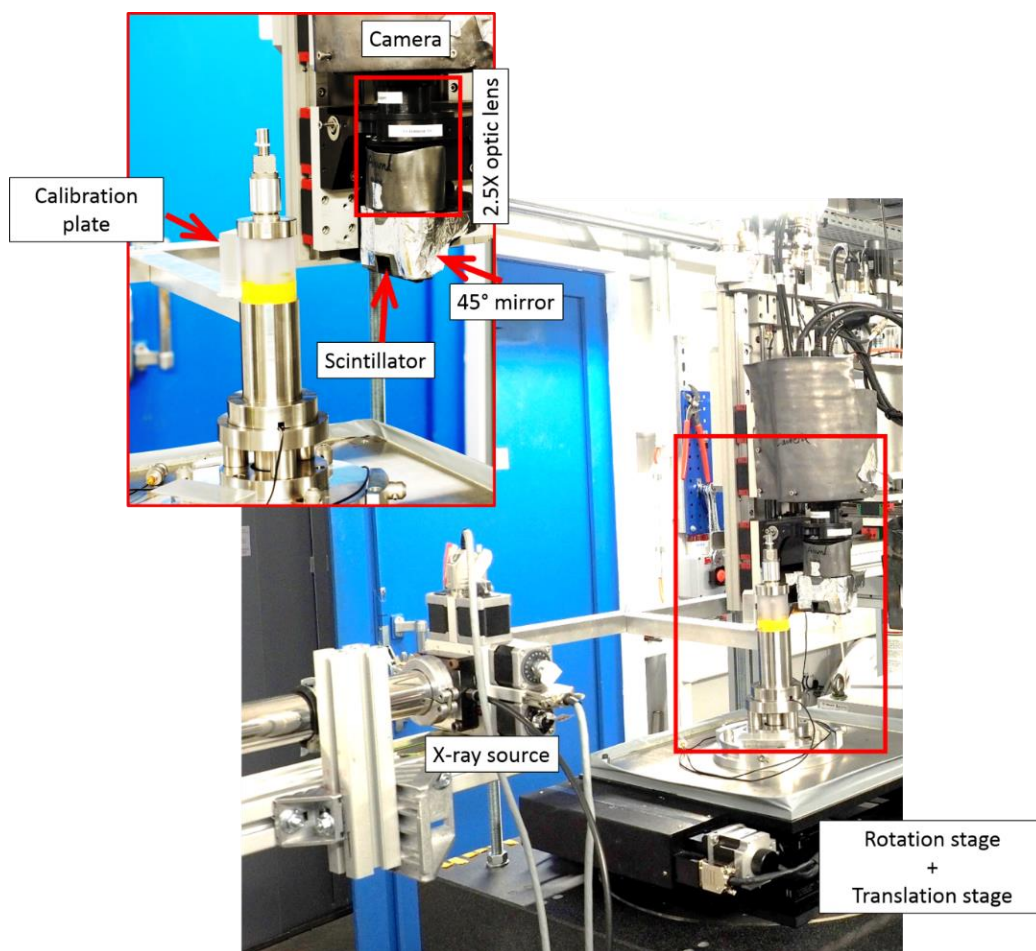
## 2.2 In situ tensile testing and data processing

### 2.2.1 Loading devices and imaging parameters

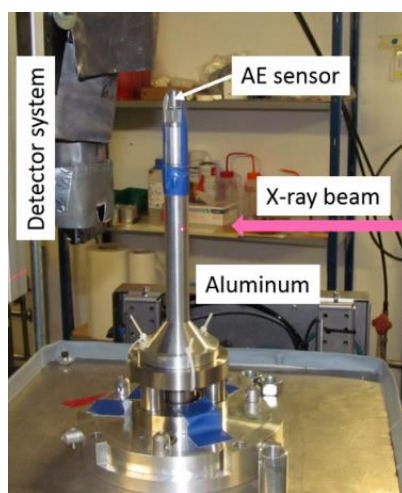
In situ experiments were performed using the  $\mu$ CT setup on the PSICHE beamline of SOLEIL synchrotron (Figure 3). Two series of tests were conducted using different loading rigs (see Figure 3 a and b). The loading device was composed of two parts: an actuator (not shown in the figure) that is placed beneath the rotation/translation stage and an upper part that transmits the tensile load to the sample inside it. The first test series involved only one test on a 45° tube. An upper part made of aluminium (Figure 3.b) was used. During this test, a heating effect of the beam on the aluminium part was observed inducing a non-negligible movement of the sample during the scan. This issue was alleviated by reducing the beam flux and exposure time. Therefore, the aluminium upper part has been replaced by a different design with a polycarbonate window (see Figure 3.a) for the second series of tests, during which tubes with 30° and 60° braiding angles were tested. A more detailed description of these two designs can be found in [28], Chapter 2.

A pink beam, with energies centred at about 45 keV, was used for both series of tests. The scan parameters were similar for all the tests and they are listed in Table 1. The main difference between the two series was the number of radiographs and the exposure time per frame: a shorter exposure time was used for the first series but compensated by a larger number of radiographs. In order to achieve a larger vertical field of view, each sample was scanned at two adjacent vertical positions, except the 60° tube whose axial architecture period was shorter than the other tubes so that three axial periods could be covered by one single image. Each two vertically adjacent images shared an overlapping zone, so that they could be stitched afterwards. The stitched images contained three axial periods for the 45°

tube and two for the 30° tube. The whole circumference of each tube was included in the field of view. Therefore, the observations covered 12 braid patterns (i.e. 3 in the axial direction, 4 in the circumference) for the 45° and 60° tubes and 8 for the 30° tube (i.e. 2 x 4).



(a)



(b)

Figure 3. (a) In situ  $\mu$ CT setup at SOLEIL synchrotron (PSICHE beamline) used for the second series of tests, with the zoomed-in image showing the upper part with a polycarbonate window. (b) The aluminium upper part of the loading device used for the first series of test.

Series	Tube name	Reconstructed image dimension (voxel)	Number of radiographs	Exposure time (ms/f)	Voxel size ( $\mu\text{m}$ )
#1	45°	2048x2048x1024	12000	15	2.60
#2	30°	2048x2048x1120	4000	80	2.85
	60°	2048x2048x1120	4000	120	2.85

Table 1. Image acquisition parameters for the two series of tests

### 2.2.2 Reconstructed images

3D images were reconstructed using PyHST2 code [29], saved in 32-bit float format, and then converted into 8-bit unsigned integer format for further post-processing. An example of the reconstructed images is given in Figure 4. Although the voxel size was smaller than the average fibre diameter ( $\sim 12 \mu\text{m}$ ), fibres and matrix could barely be distinguished because of their low chemical contrast (both are close to stoichiometric SiC). Macro-pores and large micro-pores could, however, be clearly seen and distinguished.

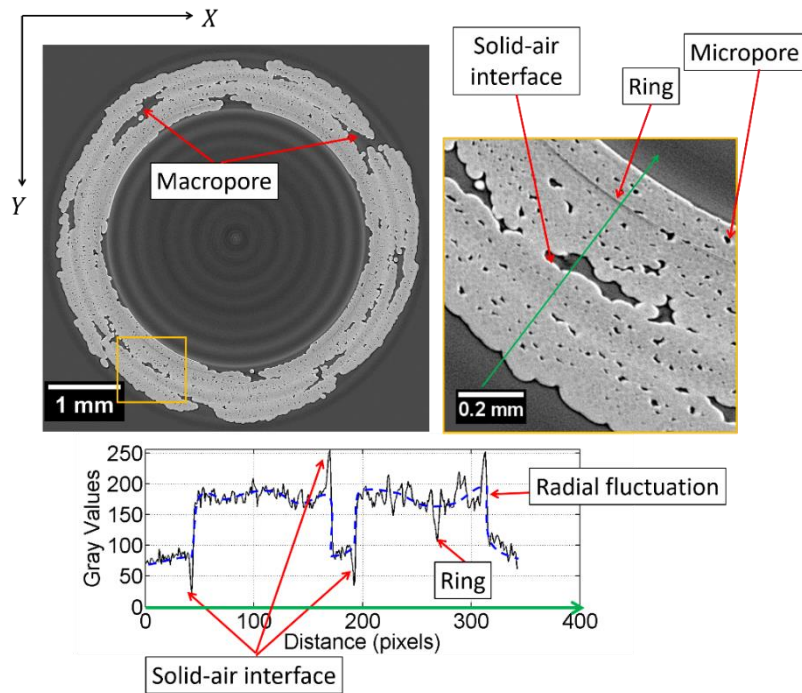


Figure 4. Reconstructed image of the 45° tube: cross-sectional slice and grey-level profile along the green line. Artefacts are highlighted by the grey-level profile along the green line: over-contrasted solid-air interface, ring, radial fluctuations of brightness.

The signal-to-noise ratios (SNRs) of the images for the three tubes were quantified using the formula:

$$SNR = \frac{v^{SiC} - v^{pore}}{\max\{std^{SiC}, std^{pore}\}} \quad (1)$$

where  $v^{SiC}$  and  $v^{pore}$  denote the average grey levels of SiC solid and macropore zones, respectively;  $std^{SiC}$  and  $std^{pore}$  are the corresponding standard deviations. In practice, several typical solid and macropore zones have been manually chosen within ImageJ to determine these values. The results showed that SNRs for all images varied between 7.0 and 8.1, suggesting a good and similar image quality for the three tubes. However, the reconstructed images still suffered from some artefacts, as highlighted in [Figure 4](#). The procedures proposed by [27] were used to reduce their effect on crack detection and quantification.

### 2.3 DVC analysis and strain evaluation

DVC was conducted on the in situ images to evaluate the 3D displacement field, from which the deformation heterogeneity through the tube thickness was examined. The in-house DVC software CMV3D [30] based on local correlation method was used. The correlation points were defined with respect to the cylindrical coordinates  $(r, \theta, z)$ . The tube thickness was discretized into a series of radial layers, each of them being represented by the correlation points having the same radial coordinate. Average strains over each radial layer were evaluated by finding the best fitting of a per-layer homogeneous deformation model to the DVC-measured displacements of the related correlation points. This procedure provided profiles of the principal strain components  $\varepsilon_{rr}, \varepsilon_{\theta\theta}, \varepsilon_{zz}$  in the through-thickness (or radial) direction. A detailed description of this procedure can be found in [27,28].

### 2.4 Crack detection and quantification

A DVC-based image subtraction technique [24] was used to detect the open cracks in the composites. This technique consists in computing the difference between the reference image and an image calculated from the deformed image according to DVC-measured displacement field. Thus, the microstructural features that disturb the crack segmentation, such as pores, are removed from the obtained image. After the image subtraction, several specific procedures were applied to remove or reduce the effects of artefacts on the detection of cracks (see [27,28]for details) . Then, the cracks created from mechanical loading can be extracted from a simple grey-level thresholding.

This crack detection procedure enables extracting very complex and numerous crack networks embedded in complex microstructures. This could not have been achieved by a direct grey-level thresholding because of the similarity of grey levels between pores and cracks in the images. As all other image based characterisation methods, the crack detection procedure cannot capture all cracks in the material due to the limitations on spatial resolution and SNRs of  $\mu$ CT images. In the present study, cracks with opening smaller than 0.2 voxel



(0.5~0.6  $\mu\text{m}$ ) are omitted. In fact, such detectability proposes a compromise between the large field of view for more statistics, and the precision of crack detection that is lower than the expected crack openings in general (a few micrometres [17]). Hence, the detected crack networks, with complex geometries, provide comprehensive arguments for better understanding the damage evolution in SiC/SiC composite tubes.

Once the crack networks were detected, their spatial geometries were quantified with a method based on image grey levels [27]. This procedure decomposed the volume of cracks into 3D surface and local opening, which can be used as two damage parameters that are more relevant than a simple voxel counting.

## 2.5 FFT simulation

Due to the limitation on the temporal resolution of in situ  $\mu\text{CT}$  scans, it is difficult to capture the exact initiation of damage. Moreover, due to the limitation on the spatial resolution, it is also likely that some of the cracks, created at the onset of non-linearity of the stress-strain curves, have been missing from the detection at the first loading steps of the in situ tests. As discussed in our previous work [25], to alleviate these limitations, we performed numerical simulations with the realistic microstructures to evaluate the elastic stress fields. The simulation results were then analysed together with the cracks detected from the in situ experiments. These cracks had been detected shortly after the beginning of the non-linearity in [Figure 2](#), so they are believed to be mostly the extension of the first cracks that were created at the onset of the non-linearity.

Compared to classical Finite Element codes, FFT-based methods (and codes) have a great advantage in image-based modelling with full-resolution that usually contains over billions of voxels [25,31]. The images at reference (unloaded) stage of the in situ experiments were directly used to generate the unit cells without reducing the resolutions. Since the fibres and matrix were undistinguishable in our images, they were considered as the same isotropic material with Young's modulus of 400 GPa and Poisson's ratio of 0.2. It has been discussed in [25] that this consideration is reasonable for elastic regime owing to the similarity of elastic properties between fibres and matrix and to the very thin thickness of pyrocarbon interphases. The pore voxels were assigned an elastic modulus of zero. To compare the simulations to the experiments, we applied a macroscopic loading condition of axial strain with a nominal value of 1%. The local stress fields of the real microstructures were calculated using linear elastic law. Maximum principal stress was then calculated at each voxel. The use of high-resolution images in the numerical models made the local stress fields smooth and insensitive to the regular voxel-type discretization [25]. Every simulation was conducted over the French supercomputer CCRT Cobalt [32] using more than 1600 cores. By virtue of the massively parallel implementation of the in-house code AMITEX [26], computations with more than 7 billion voxels were completed within approximately 20 min.

### 3. Results and discussions

#### 3.1 Unwrapping and projection

The information obtained from either the experimental observations (braid architectures and detected crack networks) or the FFT simulations (stress fields) are expressed over tubular shape. Visualising and interpreting them are not trivial in 3D. Therefore, we choose to firstly “unwrap” the tubular shape into a cuboid one. The unwrapping procedure consists in remapping each cross-sectional slice from polar to Cartesian coordinates using 2D interpolation. Linear and nearest-neighbour interpolations are used for grey-level (and stress field) images and binary images (e.g. detected cracks), respectively.

In the cuboid configuration, the tube thickness is divided into four sublayers according to the radial profiles of macro- and micro-pores (Figure 5). The information is then projected within each sublayer along the through-thickness direction. This radial projection consists in averaging the stress values and summing the detected crack voxels. These procedures of unwrapping and radial sublayer projection allow us to simplify the 3D visualisation into 2D without losing information in the composite bulks.

Figure 5 also illustrates some characteristic regions of a braided structure. “Parallel tows” and “cross-over tows” refer to as the two adjacent fibre tows with the same orientation and different orientations, respectively. Accordingly, “parallel tow interface” and “cross-over tow interface” refer to as the interfaces between two parallel tows and between two cross-over tows, respectively. These vocabularies will be used for discussing the results.

#### 3.2 First look at the detected cracks: two crack families with different orientations

Figure 6 shows the 500 largest cracks detected in each tube, giving a global idea about the 3D crack networks in the tubular configuration. Each crack voxel has been associated to an orientation vector (opening direction) that is determined from the inertia tensor of the local region surrounding the considered crack voxel [27,28]. We characterise the crack orientation by the angle  $\gamma_r$  defined between the opening direction of the crack and the local radial axis  $e_r$ . According to this parameter, the crack voxels in the 30° and 45° tubes are classified into two groups:

- in-plane cracks, whose opening direction is in the radial direction (ideally  $\gamma = 0$ , extended to  $\gamma < \pi/4$ ). Although the term “in-plane” is not rigorously correct for a tubular composite, we use it to describe the cracks that propagate along the tube wall;
- circumferential cracks, which are generally opening along the axial direction (ideally  $\gamma = \pi/2$ , extended to  $\gamma > \pi/4$ ), and mainly propagate along the tube circumference.

For the 60° tube, there seem to be many onsets of in-plane cracks, but their extensions are very small. This makes the crack classification very sensitive to the local fluctuations. Therefore, we keep the cracks in the 60° tube unclassified in further analyses. It might be possible that the cracks in the 60° tube have not fully propagated or open (comparatively to the two other tubes), since the strain of the last loading step is well below the expected strain

to failure. In fact, because of its flat nonlinear behaviour (see Figure 2), loading the 60° tube close to the ultimate strain level is more difficult than the two other tubes.

The 3D visualisation of Figure 6 suggests that the two families of cracks are seemingly connected to each other, and one in-plane crack may be connected to at least one circumferential crack in the 30° and 45° tubes. Waviness is observed on the circumferential cracks in the three tubes, and the waviness amplitude clearly increases with braiding angle. In further analyses, the detected cracks will be superimposed onto the braided microstructures in the unwrapped configuration. Only the external sublayer L4 (see Figure 5) of each tube will be presented to illustrate the damage initiation and propagation. Similar conclusions can be deduced from other sublayers (see supplementary materials).

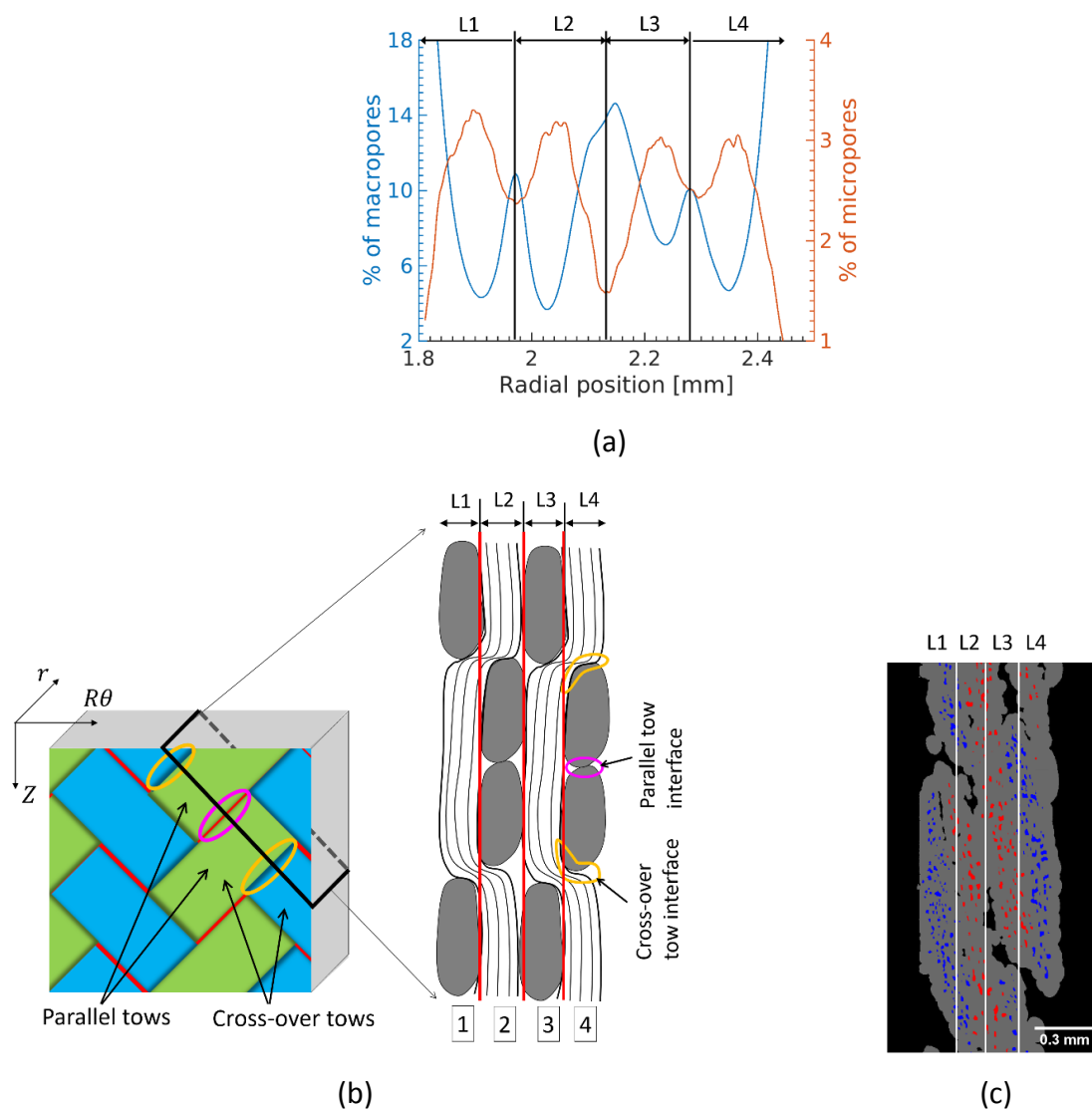


Figure 5. Through-thickness dividing: (a) radial profiles of volume fractions of macro- and micropores in the 45° tube; (b) schematic illustrating the through-thickness architecture with four sublayers, together with the definitions of some characteristic regions; (c) longitudinal slice of the 45° tube, where two groups of micropores are coloured according to their orientations (+/- 45°).

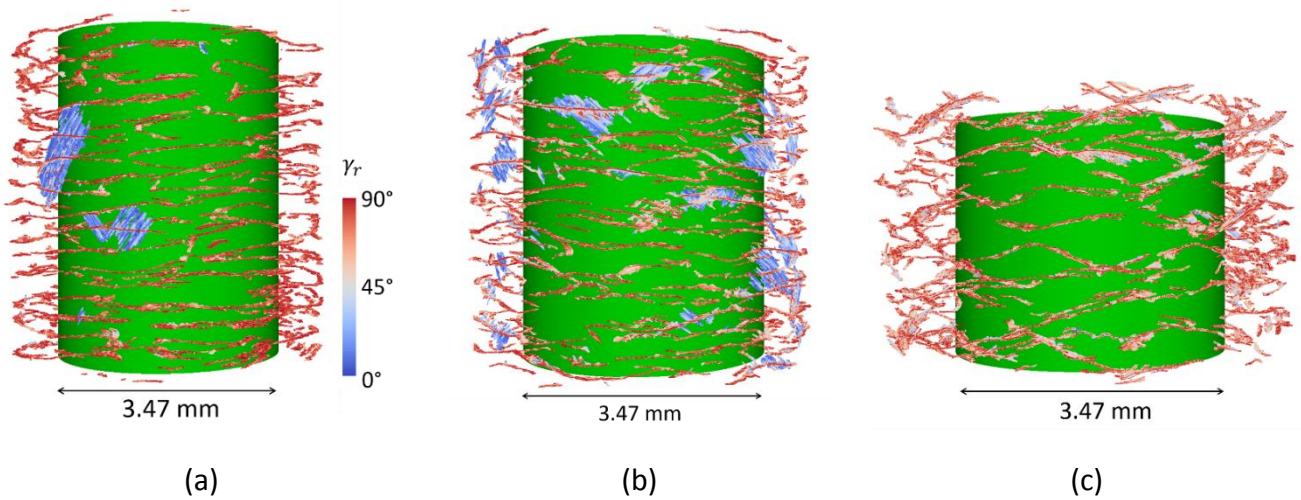


Figure 6. 3D visualisation of the 500 largest cracks detected at the last loading step in each tube: (a) 30°, (b) 45°, (c) 60°. The colour map represents the characteristic angle  $\gamma_r$ . For that sake of visibility, a green cylinder is added to represent the boundary surface between the two braided layers in each tube. The corresponding video animations can be found in the supplementary materials.

### 3.3 Damage initiation

The maps of the simulated maximum principal stresses are given in Figure 7, with the cracks detected at early loading steps superimposed. The values of maximum principal stresses have been normalized by the average axial stress in each tube, so Figure 7 can be interpreted as fields of stress concentration factors. If we assume that each crack, detected at early loading steps, corresponds to one independent event, then the number of observations is over hundreds, providing a good statistical argument for analysing the damage initiation of the studied materials.

In Figure 7, most of the experimentally detected cracks are connected to at least one stress concentration zones near tow interfaces. This suggests that the detected cracks should indeed be the extensions of those responsible for the onset of nonlinearity in the macroscopic stress-strain curves in Figure 2. Furthermore, this observation is similar for the three tubes, indicating that damage initiates always at tow interfaces regardless the braiding angle. Similar crack onset location has also been suspected from the strain field measured from a triaxial braided SiC/SiC tube under internal pressure in [20], though in which only a small zone of the composite tube has been analysed. On the other hand, if we compare the three tubes, a larger braiding angle induces higher stress heterogeneity. This difference in stress heterogeneity might stem from two microstructural reasons: (i) the tortuosity (or out-of-plane undulation) of tows is higher for a larger braiding angle due to the manufacturing process (Chapter 4.1 in [28]), hence inducing higher stress concentrations; (ii) the elongation directions of narrow pore edges follow the directions of fibre tows, hence the larger the braiding angle, the greater the angle between the pore elongation direction and the loading axis, making the stress concentrations higher. Up to now, the high-resolution simulations together with a well-correlated observation of the experimentally detected cracks appear to provide a more convincing explanation of the effect of braiding angle on the macroscopic elastic limit (Figure 2): a larger braiding angle induces a higher degree of stress concentration at tow interfaces, hence resulting in a lower macroscopic elastic limit.

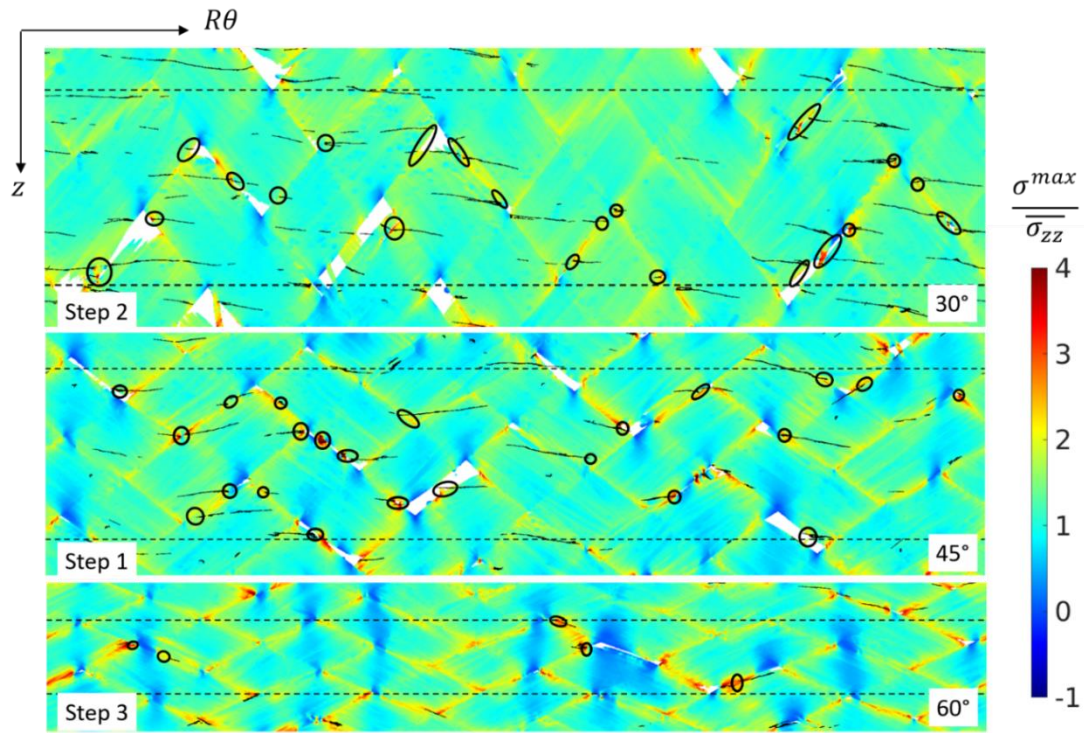


Figure 7. Radial projections (averages) of the values of maximum principal stresses in the three tubes. Cracks detected in each tube at early loading step (indicated in each graph) are superimposed. The circles indicate the crack tips connecting to stress concentration zones. Dashed lines frame the central parts where edge effects of numerical simulations are negligible [24].

### 3.4 Damage propagation scenarios (qualitative observation)

#### 3.4.1 Damage in the 45° tube: intra-tow cracking

The 45° tube is considered as reference material. Figure 8 shows the radial projections of circumferential and in-plane cracks in the external sublayer of the 45° tube.

Overall, circumferential cracks are detected prior to in-plane cracks. After being initiated near tow interfaces, they grow in the circumferential direction and may cross through the interfaces to the neighbouring fibre tows. Their opening direction is generally parallel to the loading direction (along the tube axis), but some fluctuations of this orientation (waviness) can be observed, especially near the tow interfaces. An example is marked in Figure 8 (step 5) by the three white arrows showing the local normal directions of the considered crack.

In-plane cracks seem to appear after the circumferential cracks have significantly grown. Their propagation is mostly stopped at the parallel tow interfaces. In order to check how in-plane cracks propagate in tows further than the considered sublayer (L4), the projection of the underneath part (L3) is also shown in Figure 8 for step 5. It suggests that in-plane cracks are stopped by the cross-over tow interfaces, *i.e.* they do not propagate between the two adjacent sublayers L3 and L4. As highlighted by the light blue arrows, an in-plane crack can be seen in L4 but does not appear in L3. This suggests that no inter-tow damage (cracks in-between tows) occurs in the 45° tube. Let us note that the real braid architecture exhibits spatial fluctuations, leading to small biases in the sublayer dividing, which can explain some spurious in-plane cracks observed in L3 (an example is pointed out by the black arrow in L3).

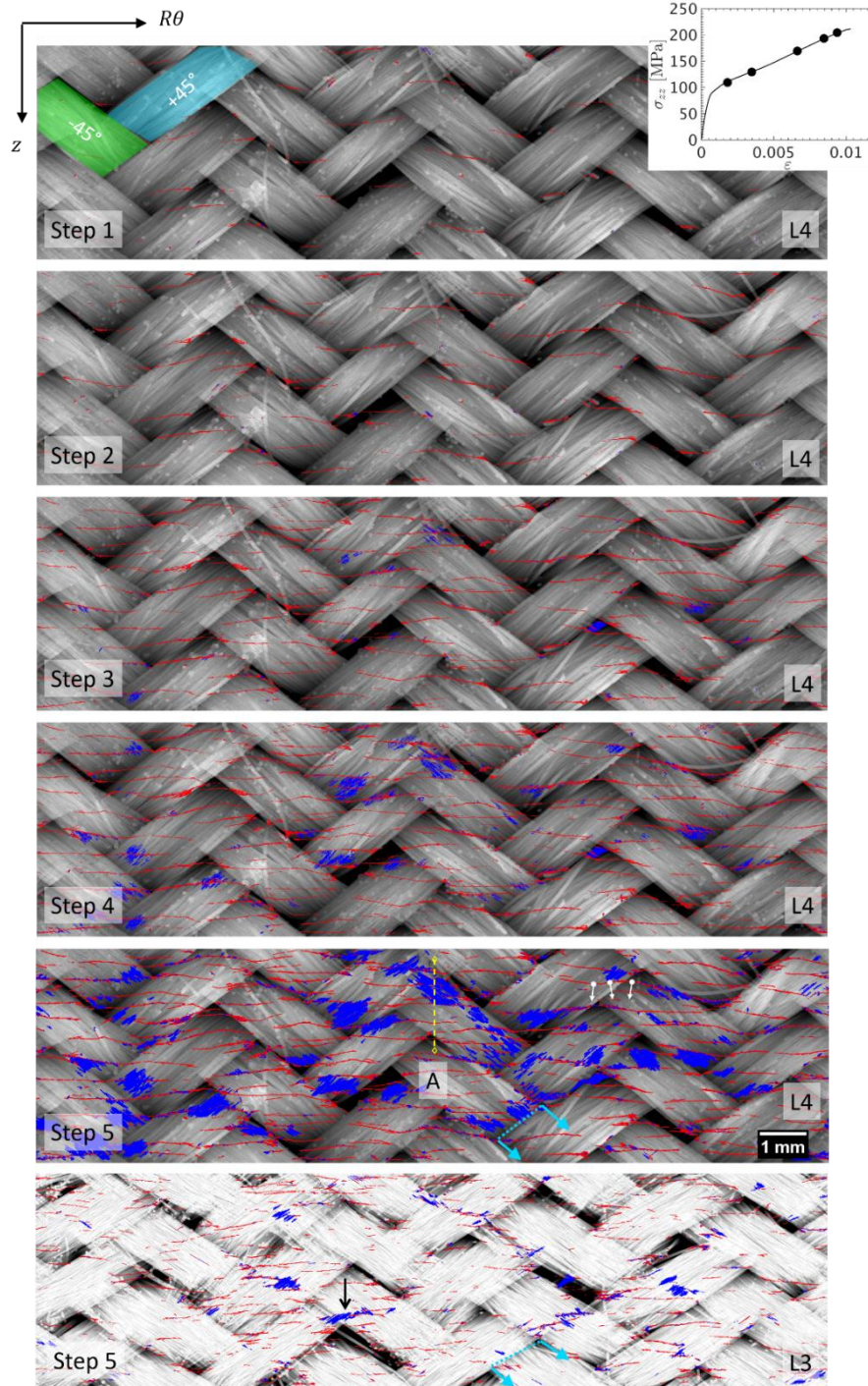


Figure 8. Radial projections of the circumferential (red) and in-plane (blue) cracks detected in the sublayer L4 (for five loading steps) and the sublayer L3 (for the fifth loading step) of the 45° tube. The corresponding braid architecture is also projected and superimposed. The three white arrows (step 5, L4) address the variation of crack orientation; the light blue arrows (step 5, L4 and L3) mark out one same tow in the two adjacent sublayers; the yellow dashed line (step 5, L4) marks out the segment along which the longitudinal slice is made in Figure 9; and the black arrow (step 5, L3) points out an in-plane crack observed in L3 due to the spatial fluctuation of braid architecture.

To check the connection between in-plane and circumferential cracks suggested by the radial projections, one longitudinal slice in  $rz$ -plane is shown in Figure 9 for each loading step. A circumferential crack appears first in the peripheral matrix of the outer free surface of the tube, and starts to be deflected at the third loading step. The crack then becomes an in-plane crack. Such scenario is observed for most of the in-plane cracks. This suggests that in-plane cracks might come from the deflection of circumferential cracks within fibre tows. Combining the observations of radial projections and the longitudinal slices of these in-plane cracks, we can conclude that the in-plane cracks propagate inside tows, but not in-between tows. This intra-tow location is also confirmed by observing 2D cross-sectional slices (Figure 10). The in-plane cracks seem to propagate from one micropore to another inside the tow. Moreover, this intra-tow growth path likely separates the peripheral matrix from the centre region of the tow for some in-plane cracks (white arrows in Figure 10), and appears in the centre of tows for others (light blue arrows in Figure 10). These in-plane cracks are suspected to be related to a slight fibre tow reorientation effect that has been evidenced from surface observations in [17] mentioning a so-called ‘textile effect’.

Furthermore, the circumferential cracks have not been detected inside the tows. To confirm this, we project a small volume around a typical circumferential crack along the axial direction and the result is shown in Figure 11 for different loading levels. Assuming the micropores are mostly embedded among fibres inside tows, the projection of micropores helps to distinguish the centre region from the peripheral matrix of tows. The crack propagation scenario mentioned above is confirmed by these axial projections as well: first a circumferential crack appears in the peripheral matrix, and then it grows mainly in the circumferential direction. It propagates very slightly in the radial direction, and then it is deflected into the in-plane crack (blue) along a single tow. No circumferential crack is observed inside the tow. Given the spatial resolution and grey-level contrast in the present XCT images, the crack detection procedure is able to detect cracks with opening larger than  $0.1\sim 0.2$  voxels ( $0.3\sim 0.5\ \mu\text{m}$ ) (see, [27,28]). This detectability should be good enough to detect most matrix cracks. However, it is still possible that the detection procedure missed some tiny cracks with small openings inside tows. For instance, if the matrix among fibres has very limited volume, the related cracks might have been considered as random noises and removed from the detection procedure.

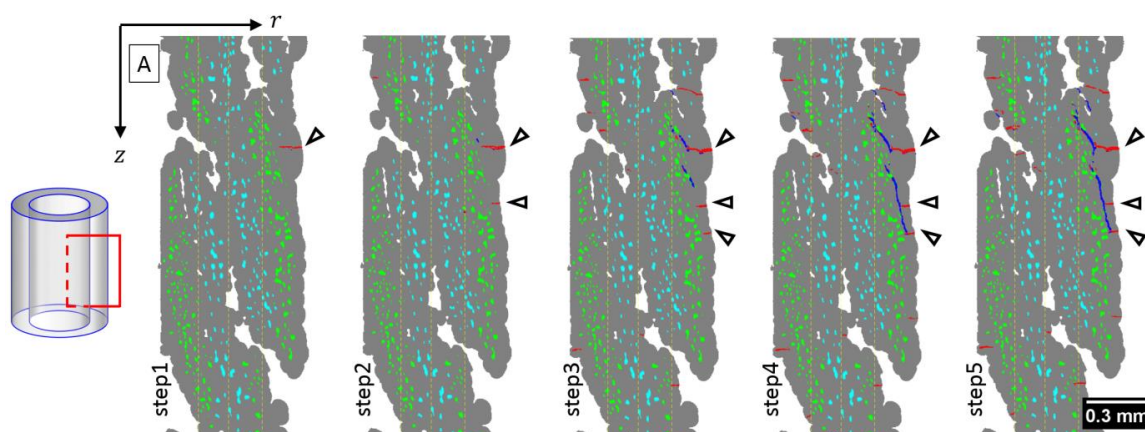


Figure 9. Longitudinal slices ( $rz$ -plane) of the  $45^\circ$  tube along the segment A (defined in Figure 8), showing the circumferential (red) and in-plane (blue) cracks at every loading step. The micropores are coloured differently according to their orientations ( $\pm 45^\circ$ , light blue and green respectively), so that the braid architecture can be recognized.

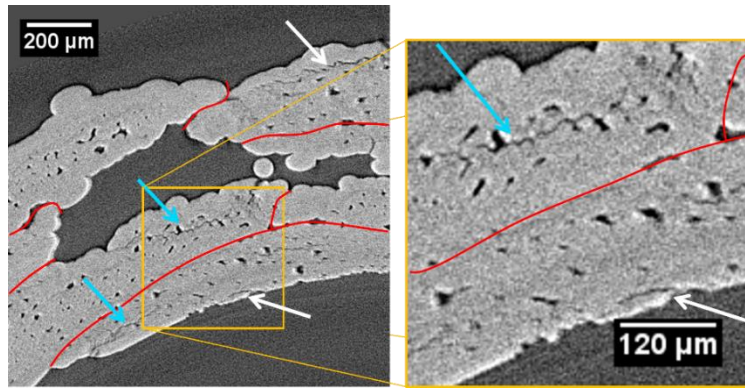


Figure 10. Cross-sectional slice showing in-plane cracks appearing at different radial positions (pointed by arrows). Tow boundaries are marked by red lines.

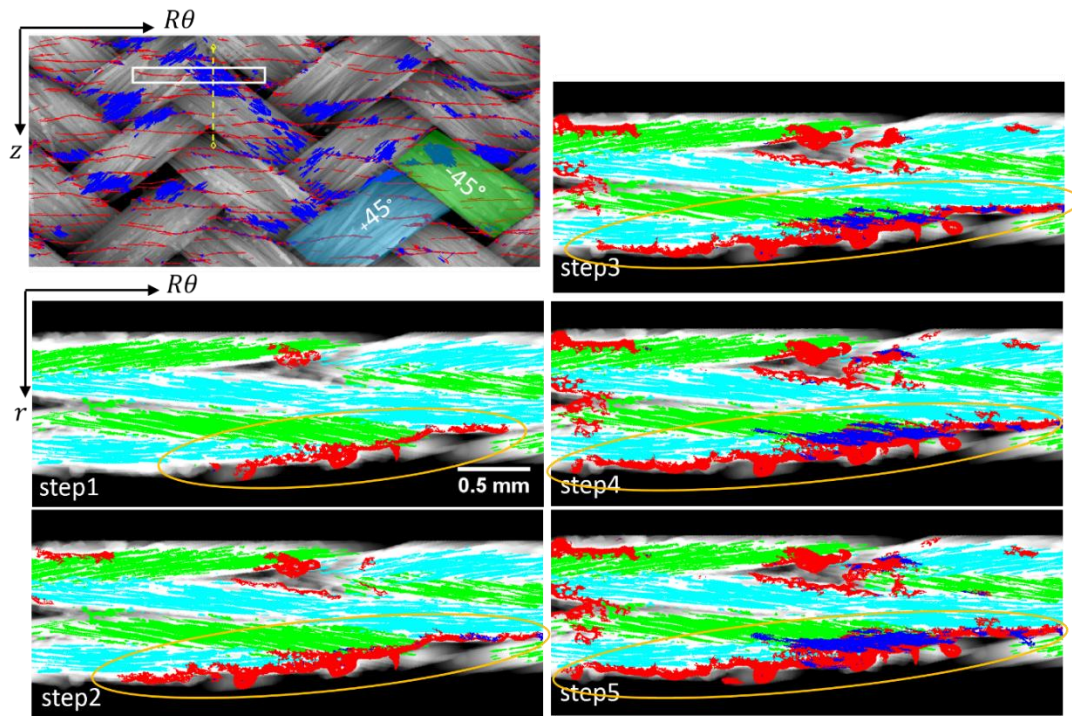


Figure 11. Axial projection of a small volume in the 45° tube around a chosen crack with circumferential (red) and in-plane (blue) cracks distinguished. The location of the projected volume is indicated in the radial projection at the top left of the figure. Circled zone is discussed in the main text.



### 3.4.2 Damage in the 30° tube: intra-tow cracking

In the 30° tube, circumferential and in-plane cracks are also observed, and their propagation scenario is similar to that in the 45° tube. Their projections along the radial direction within the external sublayer (L4) are shown in Figure 12. The circumferential cracks propagate along the tube circumference since the first loading step, which is at the beginning of the nonlinear regime. They can also cross through interfaces from one tow to the neighbouring ones, but their growth path is straighter than that in the 45° tube.

The in-plane cracks are detected much later ( $\sim 0.55\%$  of axial strain, *i.e.*  $\sim 80\%$  of the ultimate strain) and they are localized in only three tows. The in-plane cracks also stop to propagate at the tow interfaces, as shown by the radial projection in the underneath sublayer L3 (Figure 12). Although a small in-plane crack observed in L3 (circled in the figure) seems to have originated from the propagation of that in L4, its growth is very limited even for the last loading step.

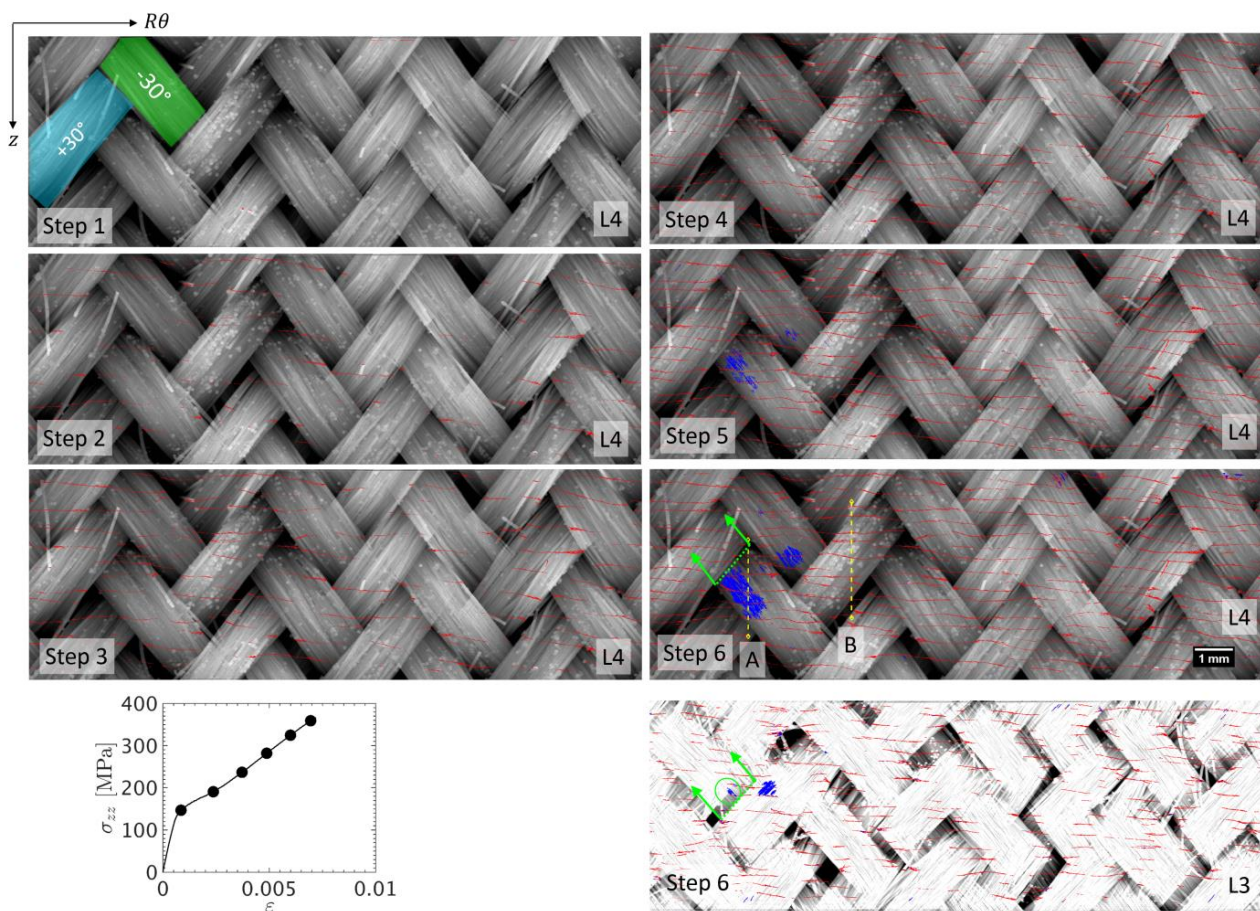


Figure 12. Radial projections of the circumferential (red) and in-plane (blue) cracks detected in the sublayer L4 (for the six loading steps) and the sublayer L3 (for the sixth loading step) of the 30° tube superimposed to the projected braided architectures. The green arrows (step 6, L4 and L3) mark out one same tow in the two adjacent sublayers and the yellow dashed lines (step 6, L4) mark out the segments along which the longitudinal slices are shown in Figure 13.

In order to observe the crack growth through the tube thickness, the longitudinal slices in  $rz$ -plane along two segments A and B (defined in [Figure 12](#)) are shown in [Figure 13](#). In the slice along the segment A, the deflection of circumferential cracks into in-plane cracks is shown, similarly to what has been observed in the  $45^\circ$  tube. The in-plane cracks in the  $30^\circ$  tube also stem from the deflection of the circumferential cracks and their growth path is inside, but not in-between, tows. In the slices along the segment B, the circumferential cracks exhibit a relatively uniform distribution along the axial direction, especially on the outer free surface of the tube. In addition, many of them can be associated with another crack that is located on the other side of the tow at the same axial position (cracks in pair, as marked by the triangles in [Figure 13](#)).

To check the propagation of circumferential cracks in the centre regions of fibre tows in the  $30^\circ$  tube, a small volume is projected along the axial direction in [Figure 14](#). Two circumferential cracks are observed independently on the two sides of the tow. Then they both grow in radial and circumferential directions. A few circumferential cracks are observed in the tow-centre region (pointed out by black arrow) when the damage is sufficiently developed (step 4,  $\sim 0.5\%$  of axial strain).

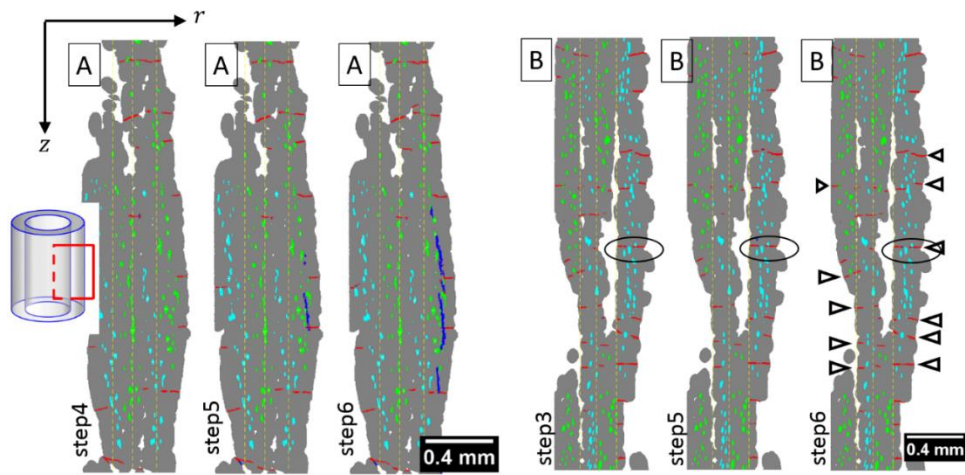


Figure 13. Longitudinal slices along the two segments A and B (see Figure 12) in the 30° tube at different loading steps. The micropores are coloured differently according to their orientation for indicating the braid architecture. The triangles point out the cracks in pair discussed in the main text, and one of them (circled) will be further discussed in Figure 14.

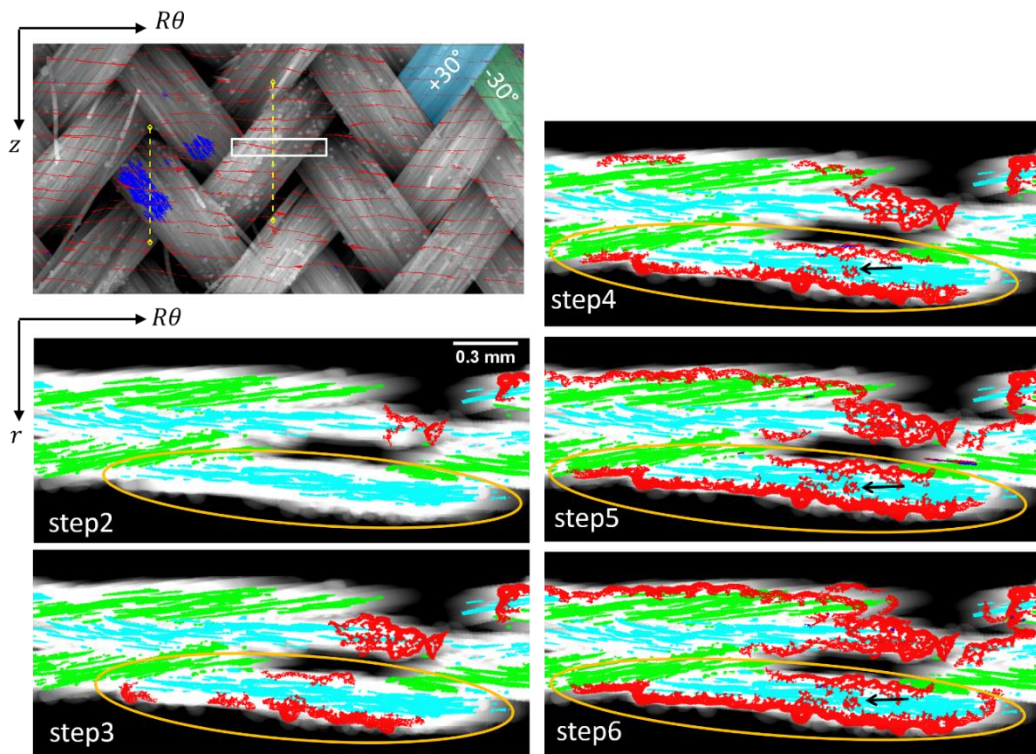


Figure 14. Axial projection of a small volume in the 30° tube around a chosen crack with circumferential (red) and in-plane (blue) cracks distinguished. The location of the projected volume is indicated in the radial projection at the top left of the figure. The braid architecture is also projected and superimposed, and the micropores are coloured differently according to their orientations (+/-30°, light blue and green respectively), so that the braid architecture can be recognized. Circled zone is discussed in the main text.

### 3.4.3 Damage in the 60° tube: inter-tow cracking

In the 60° tube, another crack propagation path is observed. We have chosen to keep the detected cracks unclassified in this tube due to the small extensions of in-plane cracks (see [section 3.2](#)). [Figure 15](#) shows the radial projections of the cracks detected in the external sublayer L4 at different loading steps. After being initiated at tow interfaces, cracks in the 60° tube grow primarily along the tow interfaces, which is clearly different from the propagation paths in the two other tubes. These inter-tow cracks change their propagation direction at the zones where three tows are intersected (triple points), e.g. if a crack grows initially along a parallel interface, its propagation direction will change to follow the neighbouring cross-over tow interface. At the last loading step, almost all the tow interfaces (parallel and cross-over) are cracked forming a zig-zag pattern. Moreover, some inter-tow cracks tend to grow inside the tows, especially those propagating along the cross-over tow interfaces, revealing complex stress distributions at these zones (an example is pointed out by arrows in [Figure 15](#)). This zig-zag growth path of the inter-tow cracks confirms the strong waviness observed in the 3D visualisation in [Figure 6](#).

To examine how these zig-zag cracks grow through the tube thickness, longitudinal slices in  $rz$ -plane along the two segments A and B (defined in [Figure 15](#)) are shown in [Figure 16](#) for different loading steps. The two series of slices show the crack propagation in the parallel and cross-over tow interfaces, respectively. Cracks significantly grow into the tube thickness along both interfaces. The growth along parallel tow interfaces (segment A) seems to be stopped by the underneath intersecting tow, because no crack deflection is observed. The growth along cross-over tow interfaces (segment B) is deviated into one of the two cross-over tows after a significant growth between them. This slight deviation makes the crack (crack 1) to join another crack on the other side of the tow (crack 2). This inter-tow damage may possibly promote the reorientation of fibre tows under axial tension.

The cracks along cross-over tow interfaces have orientations different from those of the circumferential cracks in the 30° and 45° tubes, which explains the small population of in-plane cracks observed from the 3D visualisation in the 60° tube in [Figure 6](#).

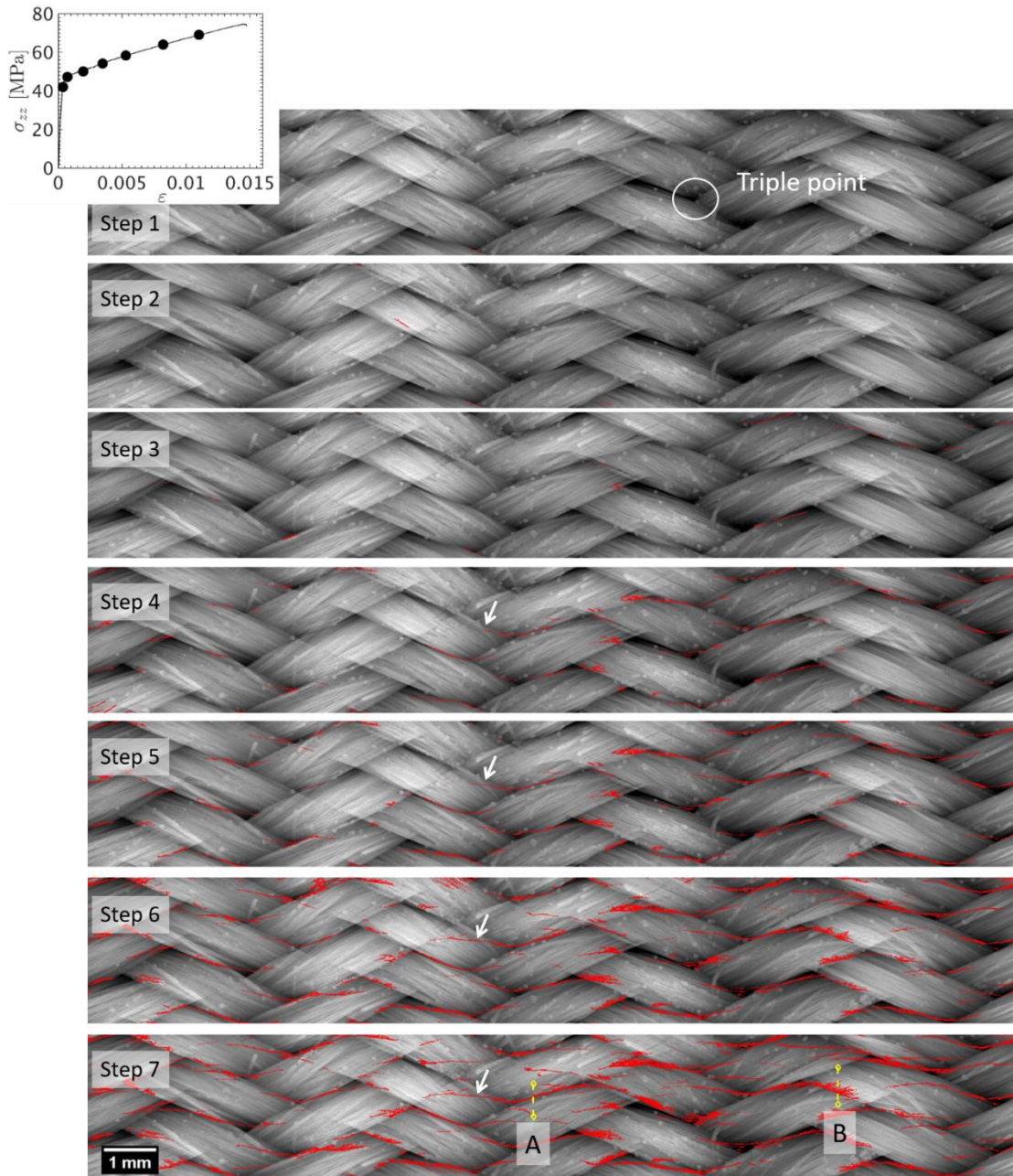


Figure 15. Radial projection of the cracks (red) detected in the sublayer L4 of the 60° tube at different loading steps, superimposed to the projected braided architecture. Arrows outline a crack that tends to grow inside a tow after its inter-tow propagation. Further longitudinal slices will be observed (in Figure 16) along the two segments A and B.

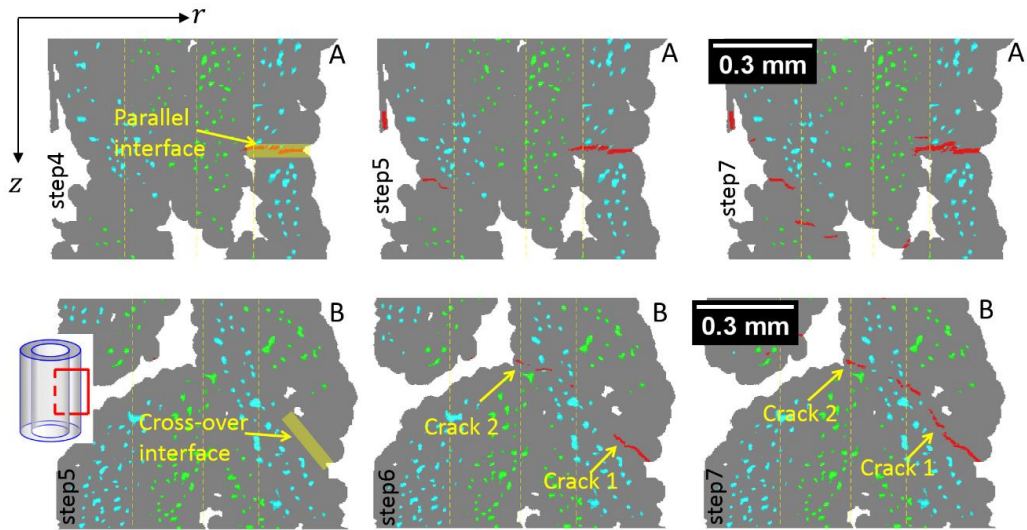


Figure 16. Longitudinal slices along the two segments A and B (defined in Figure 15) in the 60° tube at different loading steps. The micropores are coloured differently according to their orientations to visualise the braid architecture.

### 3.5 Quantitative analysis of the through-thickness heterogeneity of damage

As shown in the previous section, the crack propagation scenarios are quite different through the tube thickness. In this section, we quantify this through-thickness heterogeneity of crack networks using a recently proposed method [27]. The idea of this method is to describe the detected cracks with opening levels and surface area, instead of the crack volume usually measured by simple voxel counting. In practice, we replace crack surface area by another parameter – “crack surface density”, which is defined as the ratio between the crack surface area and the volume of solid phase in a considered region. Radial profiles of these two geometric parameters are shown in Figure 17 and 18, where the average opening  $\bar{\Delta}$  and surface density  $\rho$  have been measured at each radial position within a thin circumferential cylinder with a thickness of 2 voxels ( $\sim 5 \mu\text{m}$ ). The surface densities are not uniform through the tube thickness for all the tubes. These quantitative measurements are now interpreted in relation with the previous qualitative observations in section 3.3.

#### 3.5.1 Circumferential cracks and inter-tow cracks

##### Surface density

For the circumferential cracks in the 30° and 45° tubes, three crack populations are observed, related to the three peak positions numbered in Figure 17.a. The two populations near the inner and outer free surfaces of the tubes appear first before the third population near the boundary of the two braided layers. The locations of these crack populations are consistent with those of macropores, which suggests that the cracks appear preferably in the zones rich in macropores and peripheral matrix (see Figure 17.c). The third crack population in the 30° tube is not obvious, which may be related to the smallest out-of-plane undulation in the 30° braid, leading to less stress concentrations at the boundary of the braided layers.

For the inter-tow cracks in the 60° tube, three crack populations are found where the macropores are minimum, and at the inner free surface. This is consistent with the inter-tow propagation paths, because the radial positions of tow interfaces coincide with the zones of minimum macropores due to the out-of-plane undulations of tows (see [Figure 17.d](#)). The location of the second population (close to the inner free surface) may be explained by the fact that the inner free surface has been polished, and the corresponding tow-interfaces are very close to the inner free surface. These quantitative analyses performed over the whole tube thickness confirm the qualitative observations in the previous section.

### Opening

[Figure 17.b](#) shows the radial profiles of average crack openings, where three peaks are also observed, which are consistent with the three crack-rich positions for each tube. Overall, the cracks at tube surfaces are more open than those in the thickness. At low loading levels, there are some singular positions where very high average openings (5~8  $\mu\text{m}$ ) are observed. They are not significant because they are related to the low crack densities at these positions, making the average measurements sensitive to individual cracks with large openings.

## 3.5.2 In-plane cracks

### Surface density

The through-thickness heterogeneity of in-plane cracks in the 30° and 45° tubes is studied in [Figure 18](#). In the 45° tube, each of the two braided layers exhibits one crack population, approximately at the same relative position of the braided layer (see [Figure 18.b](#)). In the 30° tube, only one population is clearly distinguished, which is in the outer braided layer. The qualitative observations have shown that only a few localised in-plane cracks appear in the 30° tube ([Figure 12](#)). The radial positions of all the crack-rich regions in both tubes are consistent with the qualitative observations, as illustrated in [Figure 18.b](#).

Moreover, the peaks of the in-plane cracks are slightly at the left of those of circumferential cracks. In particular, no in-plane crack peak is observed in the inner braided layer of the 30° tube, where very few circumferential cracks are found (peak 2 in [Figure 17.a](#)). This confirms once again, in a more quantitative way, that in-plane cracks originate from the deviation of circumferential cracks inside fibre tows.

### Opening

Because of their localized radial positions, we choose to measure the average opening of in-plane cracks around each peak position. The measurement gauges and the results for the last loading step are given in [Figure 18.b](#). Similar average openings (1.8  $\mu\text{m}$ ) of in-plane cracks are reached in the outer braided layer for both tubes. In the 45° tube, the average opening of in-plane cracks is smaller in the outer braided layer than in the inner one (1.8  $\mu\text{m}$  versus 2.9  $\mu\text{m}$ ). The explanation of this difference is still unclear, it may result from complex interactions and stress redistributions within the damaged microstructure.

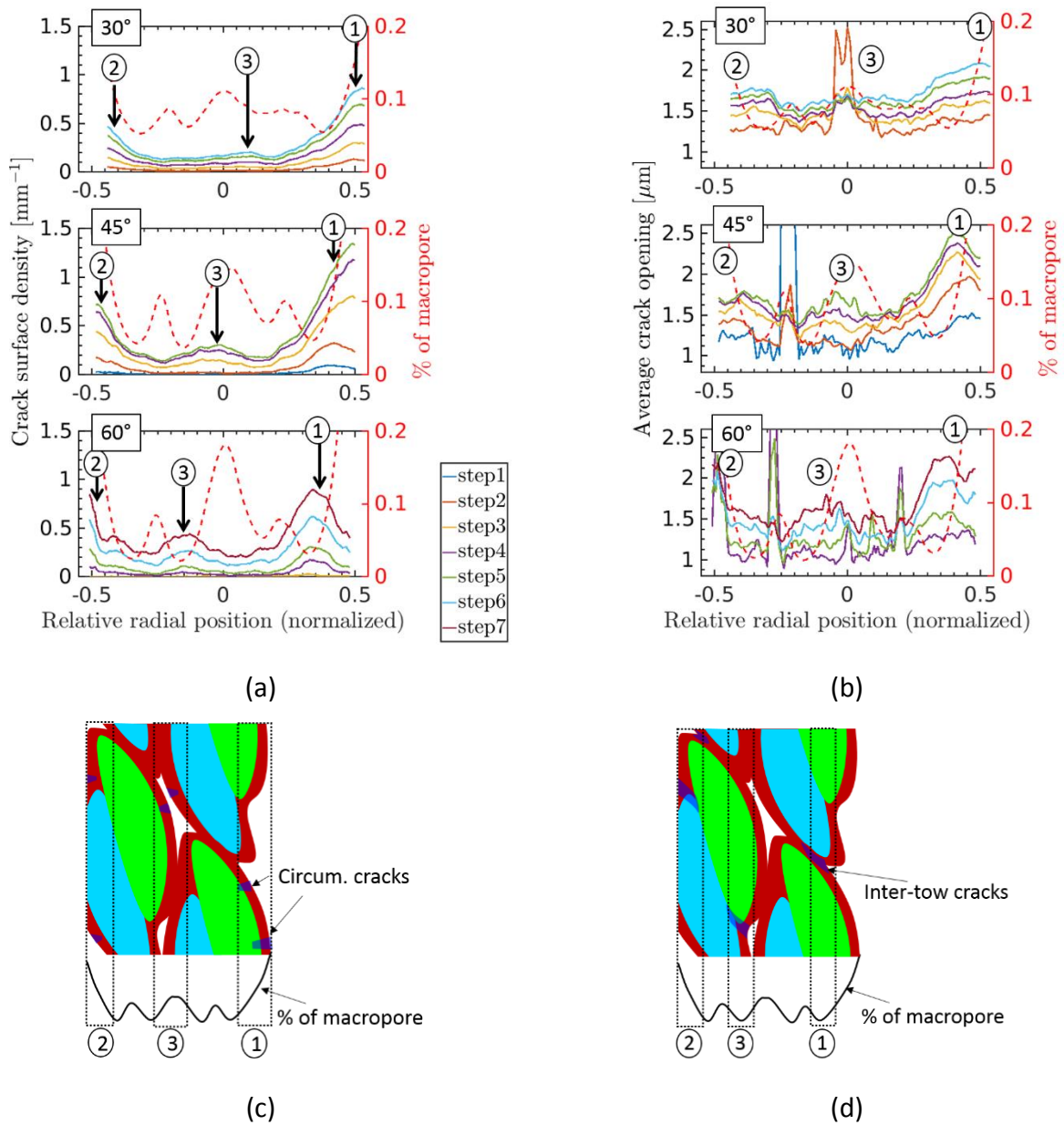


Figure 17. Radial profiles of two geometric parameters for the circumferential cracks in the 30° and 45° tubes and for all cracks in the 60° tube: (a) surface density  $\rho$ , (b) average opening  $\bar{\lambda}$ . The radial positions relative to the boundary between the two braided layers in each tube are normalized by the tube thickness, thereby the zone with  $r < 0.5$  is the inner braided layer and the zone with  $r > 0.5$  is the outer one. The three peaks in each profile are numbered (1, 2, 3). Dashed red line shows the radial profile of macropore volume fraction in each tube in order to indicate the through-thickness braid architecture. (c-d) Schematics illustrating the typical locations of circumferential cracks (for 30° and 45° tubes) and inter-tow cracks (for 60° tube) with respect to the braid architecture.



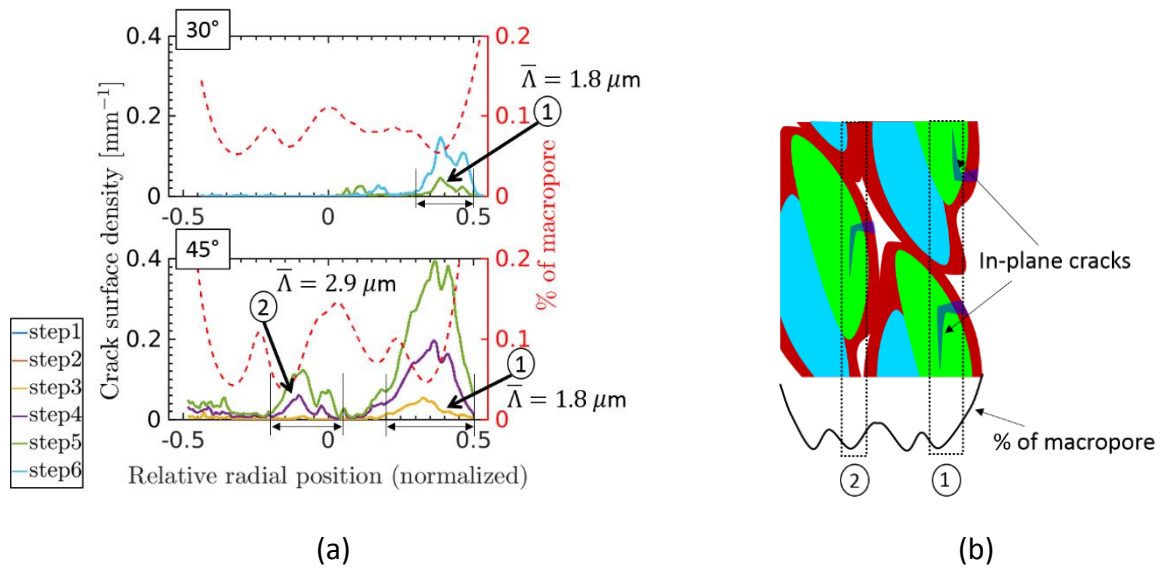


Figure 18. (a) Radial profiles of the surface density of in-plane cracks in the 30° and 45° tubes; the two populations discussed in the main text are pointed out by numbers, and their respective average opening is calculated over the marked gauges, the dashed red line shows the radial profile of macropore volume fraction in each tube. (b) Schematic illustrating the typical locations of in-plane cracks with respect to the braid architecture.

### 3.6 Unobserved damage: delamination and fibre break cluster

Since our observations have been conducted over a large field of view covering several periodic braiding patterns, it is legitimate to address some damage mechanisms that could have been expected yet are not observed in the  $\mu\text{CT}$  images.

Firstly, no delamination between the two braided layers is observed in each tube. In-plane cracks are detected in the 30° and 45° tubes, but they remain inside fibre tows and do not propagate between the two braided layers. In the 60° tube, the dominant cracks are inter-tow cracks, whose propagation seems to be limited and no delamination cracks are observed at the boundary of the two braided layers neither. The absence of inter-layer delamination is not surprising and confirms the good integrity of the SiC/SiC composites.

Secondly, fibre break clusters (multiple adjacent fibre breaks) are not observed in the three tubes, even at the last loading steps when the matrix cracks have significantly propagated. It should be noted that a fibre break producing a large enough opening ( $> 0.2$  voxel or  $\sim 0.5 \mu\text{m}$ ) should have been detected by our crack detection procedure, especially when considering the large enough fibre section area ( $\sim 150 \mu\text{m}^2$  that is covered by approximately 20 voxels). The observation on unidirectional mini-composites loaded in tension by [11] showed that fibre break openings could vary from  $7 \mu\text{m}$  ( $\sim 2.5$  voxels) up to  $50 \mu\text{m}$  ( $\sim 18$  voxels). Hence, despite the limitation ( $\sim 0.5 \mu\text{m}$ ) of the crack detection procedure, fibre break clusters should have been observed if they were present. Similar observation has also been reported by [33], concluding that fibre break clusters occur only at final burst failure of the composite, though the studied material was carbon/epoxy composite loaded in fibre axis. The unobserved fibre break clusters are crucial for micromechanical modelling, as this damage mechanism should be considered only when the material is close to its ultimate failure, but not before. In other words, in contrast to the observations on minicomposites [11] and flat specimens [23] loaded

in axis, the present observation showed no significant number of fibre breaks that contribute to the decrease of the tangent modulus of the composite. Therefore, it is likely that when a significant number of fibre breaks appear, the instability of the composite system is instantly triggered, resulting in ultimate failure. This observation is not consistent with the observation and the corresponding micromechanical modelling of UD micro-composites under tension (see e.g. [34]). The main difference that is able to explain this inconsistency is the fact that the tubes are submitted to off-axis load, while unidirectional mini-composites are loaded in-axis. It would be interesting to confirm this difference observed on fibre breaks on flat specimens loaded in- and off-axis.

### 3.7 Through-thickness variation of deformation

Figure 19 shows the strain profiles along the tube thickness measured by the DVC-based method [25,28]. Very similar profiles are observed for the three tubes. The axial strains are quasi-uniform. The hoop strains decrease from the inner to the outer surface, in terms of absolute value. An interesting point is that the radial strains are positive through the whole tube thickness. It reveals negative Poisson's ratios, which is, to the knowledge of the authors, first-time observed for such composites under tension. These through-thickness deformation profiles are now discussed based on the damage characterization presented previously.

- The positive radial strains in the 30° and 45° tubes are believed to be the consequence of the opening of in-plane cracks. For the 60° tube, on the one hand, the opening of the inter-tow cracks contributes to the positive radial strains, on the other hand, the inter-tow cracks promote the realignment of tows into the loading direction, which could induce positive out-of-plane displacements of tows, hence positive radial strains. However, one question remains open and requires further investigation: what is the local force driving the opening of in-plane cracks in the 30° and 45° tubes?
- The hoop strain is closely related to the radial strain through the formula  $\varepsilon_{\theta\theta}(r) = \left[ u_r(R_i) + \int_{R_i}^r \varepsilon_{rr}(r) dr \right] / r$ , where  $R_i$  is the inner radius of the tube. The radial displacement at the inner surface  $u_r(R_i)$  being negative due to Poisson's effect, the positive radial strains throughout the tube thickness lead to the hoop strains decreasing in absolute value from the inner to the outer tube surface. In other words, due to the tubular shape of the composite, the in-plane damage (in-plane cracks in the 30° and 45° tubes or the inter-tow cracks in the 60° tube) affects the strain distributions not only in the radial but also in the circumferential directions.
- Even though a clear through-thickness heterogeneity has been observed for both the crack surface density and crack opening in the three tubes (Figure 17), the axial strains are nearly uniform through the tube thickness. This suggests that the contribution of the detected crack opening in the axial direction should not be the only responsible of the axial nonlinear strain, especially for the region inside the tube thickness. If the question of undetected mechanisms (a part of matrix cracking but also interfacial fibre-matrix sliding) can be raised to provide a possible explanation, it must not be omitted that the pore (especially the macro-pores) may "deform" significantly within the material, especially when cracks appear. Hence, the total nonlinear strain is contributed by not only the crack openings but also the deformation of the pores.

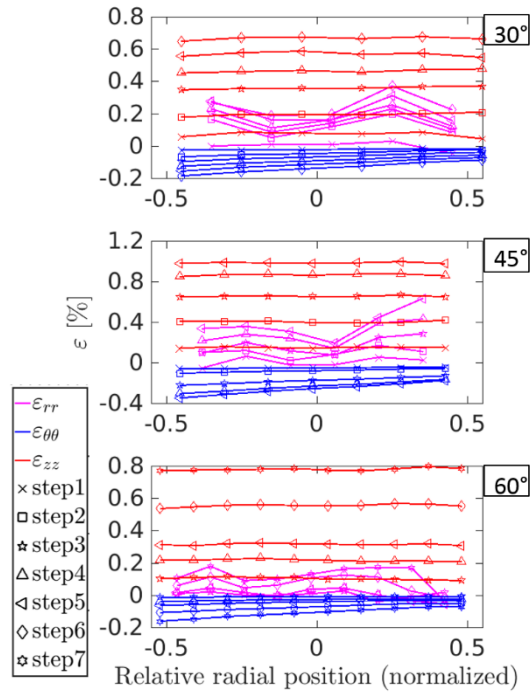


Figure 19. Radial profiles of strains in the three tubes measured by DVC based method; for the sake of clarity, the measurements of the first two loading steps for the 60° tube are not shown, but they are close to zero. The radial positions relative to the boundary between the two braided layers in each tube are normalized by the tube thickness, thereby the zone with  $r < 0$  corresponds to the inner braided layer and the zone with  $r > 0$  corresponds to the outer one.

### 3.8 Micro-macro relationship (discussion)

Now we discuss the relationship between the observed damage mechanisms and the macroscopic stress-strain curves, which also leads to a discussion on the effect of braiding angle.

According to the stress-strain curves in Figure 2, the tangent modulus of each tube is calculated and shown in Figure 20. From the evolution of their tangent moduli, the 30° and 45° tubes seem different from the 60° tube, as both tubes exhibit a slight increase of the tangent modulus at around  $\varepsilon/\varepsilon^{ultimate} \sim 0.5$ , whereas the tangent modulus of the 60° tube remains constant after  $\varepsilon/\varepsilon^{ultimate} \sim 0.1$  until final failure. This distinction between the 30° and 45° tubes and the 60° tube has also been observed from the damage propagation scenarios as presented in section 3.4: intra-two damage is dominant for the former, while inter-tow damage for the latter. Combining the qualitative and quantitative observations presented in this paper, we provide the following suggestion of interpretation attempting to bridge the mesoscopic damage observation and the macroscopic behaviour. In the 30° and 45° tubes, matrix cracks appear at the intersection zones of fibre tows and they seem to grow mainly along the circumferential direction and slightly into the tube thickness. Interestingly, as shown in Figures 17.a and 18.a, the surface density of the detected cracks kept increasing until the last loading step. This suggests that there might be no saturation of the matrix cracks in the materials. However, an increase in the macroscopic tangent modulus does exist for the 30° and 45° tubes, which could indicate that fibres have carried a significant portion of the

tensile load when matrix cracks grew to a certain extent, similarly to what is classically expected in unidirectional or flat ceramic matrix composites [34,35]. Yet, this load shared by the fibres should be statistically lower than their critical stresses since no significant fibre breaking has been observed in the 30° and 45° tubes. When the braiding angle is larger (the 60° tube), inter-tow cracking becomes dominant until the final failure of the composite. This is due to the unfavourable orientation of fibres with respect to the loading direction, making the fibres unable to carry enough load.

In Figure 21 the global surface density of the cracks detected in each tube is compared to the macroscopic axial strain. The in-plane cracks in the 30° and 45° tubes have been excluded from this analysis, because their opening is believed not contributing to the axial strain. A good correlation between the crack surface density and the axial strain can be clearly observed, which suggests that the detected cracks are relevant to reveal the major damage mechanisms contributing to the macroscopic deformations of the SiC/SiC tubes. Therefore, the qualitative and quantitative characterisations of cracks presented in this work provide a comprehensive experimental database for micromechanics-based modelling of the studied material.

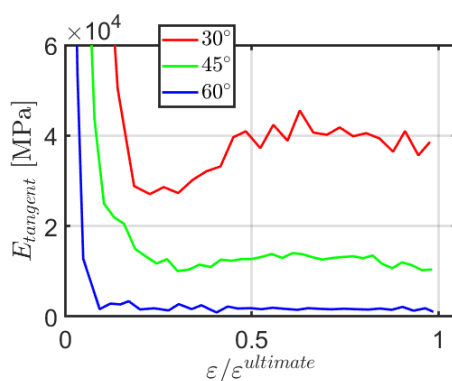


Figure 20. Tangent modulus of each tube under tension versus axial strain normalized by the ultimate value.

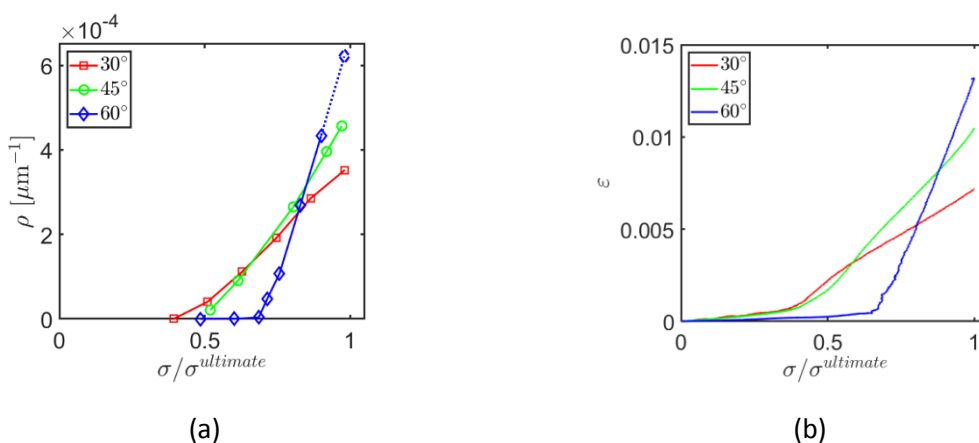


Figure 21. (a) Surface density of cracks in the three tubes with different braiding angles as function of normalized stress: circumferential cracks for the 30° and 45° tubes, all cracks for the 60° tube and the last data point (dashed line) has been plotted by extrapolating the curve. (b) Macroscopic axial strain as function of normalized stress for the three tubes.

#### 4. Conclusions

Three braided SiC/SiC composite tubes with different braiding angles have been investigated by in situ tensile tests with synchrotron  $\mu$ CT. The location of damage onsets are relatively independent on the braiding angle in the sense that they are mostly located at the tow interfaces for the three tubes. The macroscopic elastic limit decreases with the braiding angle. An explanation has been proposed through the comparison between the elastic stress fields calculated from the FFT simulations and the positions of the first detected cracks observed from the in situ tests: crack initiation occurs in the neighbourhood of stress concentration zones, and the stress concentration level increases with the braiding angle.

As for the damage growth paths, the braiding angle leads to a clear effect: intra-tow cracks in the 30° and 45° tubes and inter-tow cracks in the 60° tube. Their growth scenarios have been explicitly illustrated with respect to the braided architectures, and these have been used to explain the through-thickness variation of deformation of the composite tubes. The interpretations have been carefully drawn by keeping in mind the limitation of observation length scale. Finally, a worth-mentioning result from the micromechanical point of view is that no fibre breaks were not significantly detected during the experiments, even for the last loading levels (and it is believed that our detection limit should be able to detect them).

These damage initiation and propagation scenarios provide comprehensive experimental arguments for modelling not only the mechanical behaviours but also the thermal conductivity or oxidation properties of the SiC/SiC composites.

#### Acknowledgement

This work has been supported by the CEA/CNRS program “Défi NEEDS Matériaux”.

#### Reference

- [1] S.J. Zinkle, G.S. Was, Materials challenges in nuclear energy, *Acta Mater.* 61 (2013) 735–758. doi:10.1016/j.actamat.2012.11.004.
- [2] S.J. Zinkle, K.A. Terrani, J.C. Gehin, L.J. Ott, L.L. Snead, Accident tolerant fuels for LWRs: A perspective, *J. Nucl. Mater.* 448 (2014) 374–379. doi:10.1016/j.jnucmat.2013.12.005.
- [3] R.R. Naslain, The design of the fibre-matrix interfacial zone in ceramic matrix composites, *Compos. Part A Appl. Sci. Manuf.* 29 (1998) 1145–1155. doi:10.1016/S1359-835X(97)00128-0.
- [4] Y. Katoh, K. Ozawa, C. Shih, T. Nozawa, R.J. Shinavski, A. Hasegawa, L.L. Snead, Continuous SiC fiber, CVI SiC matrix composites for nuclear applications: Properties and irradiation effects, *J. Nucl. Mater.* 448 (2014) 448–476. doi:10.1016/j.jnucmat.2013.06.040.
- [5] R. Naslain, Design, preparation and properties of non-oxide CMCs for application in

- engines and nuclear reactors: An overview, *Compos. Sci. Technol.* 64 (2004) 155–170. doi:10.1016/S0266-3538(03)00230-6.
- [6] D. Goyal, X. Tang, J.D. Whitcomb, A.D. Kelkar, Effect of various parameters on effective engineering properties of 2 × 2 braided composites, *Mech. Adv. Mater. Struct.* 12 (2005) 113–128. doi:10.1080/15376490490493998.
- [7] E. V. Morozov, The effect of filament-winding mosaic patterns on the strength of thin-walled composite shells, *Compos. Struct.* 76 (2006) 123–129. doi:10.1016/j.compstruct.2006.06.018.
- [8] F. Bernachy-Barbe, Caractérisation des mécanismes d' endommagement et modélisation du comportement mécanique sous chargements multi-axiaux de tubes composites SiC / SiC, PhD Thesis, Ecoles des Mines de Paris, 2014.
- [9] J. Lamon, F. Rebillat, A.G. Evans, Microcomposite Test Procedure for Evaluating the Interface Properties of Ceramic Matrix Composites, *J Am. Ceram. Soc.* 78 (1995) 401–405. doi:10.1111/j.1151-2916.1995.tb08814.x.
- [10] E. Buet, C. Sauder, D. Sornin, S. Poissonnet, J.N. Rouzaud, C. Vix-Guterl, Influence of surface fibre properties and textural organization of a pyrocarbon interphase on the interfacial shear stress of SiC/SiC minicomposites reinforced with Hi-Nicalon S and Tyranno SA3 fibres, *J. Eur. Ceram. Soc.* 34 (2014) 179–188. doi:10.1016/j.jeurceramsoc.2013.08.027.
- [11] C. Chateau, L. Gélébart, M. Bornert, J. Crépin, E. Boller, C. Sauder, W. Ludwig, In situ X-ray microtomography characterization of damage in SiCf/SiC minicomposites, *Compos. Sci. Technol.* 71 (2011) 916–924. doi:10.1016/j.compscitech.2011.02.008.
- [12] H.A. Bale, A. Haboub, A.A. Macdowell, J.R. Nasiatka, D.Y. Parkinson, B.N. Cox, D.B. Marshall, R.O. Ritchie, Real-time quantitative imaging of failure events in materials under load at temperatures above 1,600°C, *Nat. Mater.* 12 (2013) 40–46. doi:10.1038/nmat3497.
- [13] G.N. Morscher, Stress-dependent matrix cracking in 2D woven SiC-fiber reinforced melt-infiltrated SiC matrix composites, *Compos. Sci. Technol.* 64 (2004) 1311–1319. doi:10.1016/j.compscitech.2003.10.022.
- [14] M. Moevus, D. Rouby, N. Godin, M. R'Mili, P. Reynaud, G. Fantozzi, G. Farizy, Analysis of damage mechanisms and associated acoustic emission in two SiC/[Si-B-C] composites exhibiting different tensile behaviours. Part I: Damage patterns and acoustic emission activity, *Compos. Sci. Technol.* 68 (2008) 1250–1257. doi:10.1016/j.compscitech.2007.12.001.
- [15] L. Gélébart, C. Chateau, M. Bornert, J. Crépin, E. Boller, X-ray tomographic characterization of the macroscopic porosity of chemical vapor infiltration SiC/SiC composites: Effects on the elastic behavior, *Int. J. Appl. Ceram. Technol.* 7 (2010) 348–360. doi:10.1111/j.1744-7402.2009.02470.x.
- [16] F. Bernachy-Barbe, L. Gélébart, M. Bornert, J. Crépin, C. Sauder, Anisotropic damage behavior of SiC/SiC composite tubes: Multiaxial testing and damage characterization, *Compos. Part A Appl. Sci. Manuf.* 76 (2015) 281–288.

- doi:10.1016/j.compositesa.2015.04.022.
- [17] F. Bernachy-Barbe, L. Gélébart, M. Bornert, J. Crépin, C. Sauder, Characterization of SiC/SiC composites damage mechanisms using Digital Image Correlation at the tow scale, *Compos. Part A Appl. Sci. Manuf.* 68 (2015) 101–109. doi:10.1016/j.compositesa.2014.09.021.
- [18] L. Saucedo-Mora, T. Lowe, S. Zhao, P.D. Lee, P.M. Mummery, T.J. Marrow, In situ observation of mechanical damage within a SiC-SiC ceramic matrix composite, *J. Nucl. Mater.* 481 (2016) 13–23. doi:10.1016/j.jnucmat.2016.09.007.
- [19] C. Simon, F. Rebillat, V. Herb, G. Camus, Monitoring damage evolution of SiCf/[SiBC]m composites using electrical resistivity: Crack density-based electromechanical modeling, *Acta Mater.* 124 (2017) 579–587. doi:10.1016/j.actamat.2016.11.036.
- [20] B.P. Croom, P. Xu, E.J. Lahoda, C.P. Deck, X. Li, Quantifying the three-dimensional damage and stress redistribution mechanisms of braided SiC/SiC composites by in situ volumetric digital image correlation, *Scr. Mater.* 130 (2017) 238–241. doi:10.1016/j.scriptamat.2016.12.021.
- [21] V. Mazars, O. Caty, G. Couégnat, A. Bouterf, S. Roux, S. Denneulin, J. Pailhès, G.L. Vignoles, Damage investigation and modeling of 3D woven ceramic matrix composites from X-ray tomography in-situ tensile tests, *Acta Mater.* 140 (2017) 130–139. doi:10.1016/j.actamat.2017.08.034.
- [22] E. Maire, P.J. Withers, Quantitative X-ray tomography, *Int. Mater. Rev.* 59 (2014) 1–43. doi:10.1179/1743280413Y.0000000023.
- [23] E. Maillet, A. Singhal, A. Hilmas, Y. Gao, Y. Zhou, G. Henson, G. Wilson, Combining in-situ synchrotron X-ray microtomography and acoustic emission to characterize damage evolution in ceramic matrix composites, *J. Eur. Ceram. Soc.* 39 (2019) 3546–3556. doi:10.1016/j.jeurceramsoc.2019.05.027.
- [24] C. Chateau, T.T. Nguyen, M. Bornert, J. Yvonnet, DVC-based image subtraction to detect microcracking in lightweight concrete, *Strain.* e12276 (2018).
- [25] Y. Chen, L. Gélébart, C. Chateau, M. Bornert, C. Sauder, A. King, Analysis of the damage initiation in a SiC/SiC composite tube from a direct comparison between large-scale numerical simulation and synchrotron X-ray micro-computed tomography, *Int. J. Solids Struct.* 161 (2019) 111–126. doi:10.1016/j.ijsolstr.2018.11.009.
- [26] AMITEX\_FFTP, (n.d.). <http://www.maisondelasimulation.fr/projects/amitex/html/>.
- [27] Y. Chen, L. Gélébart, C. Chateau, M. Bornert, A. King, P. Aïmediu, C. Sauder, 3D detection and quantitative characterization of cracks in a ceramic matrix composite tube using X-ray computed tomography, *Exp. Mech.* 60 (2020) 409–424. doi:10.1007/s11340-019-00557-5.
- [28] Y. Chen, Damage mechanisms in SiC/SiC composite tubes : three-dimensional analysis coupling tomography imaging and numerical simulation, PhD Thesis, Université Paris-Est, 2017.
- [29] A. Mirone, E. Brun, E. Gouillart, P. Tafforeau, J. Kieffer, The PyHST2 hybrid distributed

- code for high speed tomographic reconstruction with iterative reconstruction and a priori knowledge capabilities, *Nucl. Instruments Methods Phys. Res. Sect. B Beam Interact. with Mater. Atoms.* 324 (2014) 41–48.  
doi:<http://dx.doi.org/10.1016/j.nimb.2013.09.030>.
- [30] M. Bornert, J.M. Chaix, P. Doumalin, J.C. Dupré, T. Fournel, D. Jeulin, E. Maire, M. Moreaud, H. Moulinec, Mesure tridimensionnelle de champs cinématiques par imagerie volumique pour l’analyse des matériaux et des structures, *Instrumentation, Mes. Métrologie.* 4 (2004) 43–88. <http://hal.archives-ouvertes.fr/hal-00156072/en/>.
- [31] Y. Chen, D. Vasiukov, L. Gélébart, C.H. Park, A FFT solver for variational phase-field modeling of brittle fracture, *Comput. Methods Appl. Mech. Eng.* 349 (2019) 167–190.  
doi:10.1016/J.CMA.2019.02.017.
- [32] CCRT, (n.d.). <http://www-ccrt.cea.fr/index.htm>.
- [33] S.C. Garcea, I. Sinclair, S.M. Spearing, P.J. Withers, Mapping fibre failure in situ in carbon fibre reinforced polymers by fast synchrotron X-ray computed tomography, *Compos. Sci. Technol.* 149 (2017) 81–89. doi:10.1016/j.compscitech.2017.06.006.
- [34] C. Chateau, L. Gélébart, M. Bornert, J. Crépin, D. Caldemaison, C. Sauder, Modeling of damage in unidirectional ceramic matrix composites and multi-scale experimental validation on third generation SiC/SiC minicomposites, *J. Mech. Phys. Solids.* 63 (2014) 298–319. doi:10.1016/j.jmps.2013.09.001.
- [35] A.M. Hilmas, G. Henson, A. Singhal, Y. Gao, M. Schuster, In-situ observation of damage in unidirectional CMC laminates under tension, *Ceram. Int.* (2020).  
doi:10.1016/j.ceramint.2020.02.134.